Properties and Molecular docking of Antiviral to COVID-19 Chloroquine combining DFT calculations with SQMFF approach

Silvia Brandan[1], Elida Romano[1], Noureddine ISSAOUI[2], and María Manzur[1]

[1]Universidad Nacional de Tucumán
[2] Faculty of Sciences of Monastir

July 31, 2020

Abstract

Structural, electronic, topological, vibrational and molecular docking studies have been performed for both enantiomeric S(-) and R(+) forms of potential antiviral to COVID-19 chloroquine (CQ) combining DFT calculations with SQMFF methodology. Hybrid B3LYP/6-311++G** calculations in gas phase and aqueous solution predict few energy differences between both forms. Solvation energies of S(-) and R(+) form are predicted in -55.07 and 59.91 kJ/mol, respectively. Low solvation energies of both forms are justified by the presence of only four donor and acceptor H bonds groups, as compared with other antiviral agents. MK charges on the Cl1, N2, N3 and N4 atoms and AIM calculations could support the high stability of R(+) form in solution according to the higher reactivity predicted for the S(-) form in this medium. Antiviral to COVID-19 niclosamide shows higher reactivity than both forms of CQ. Complete vibrational assignments of 153 vibration modes for both forms and scaled force constants have been reported here. Reasonable concordances were found between predicted and available 1H-NMR, 13C-NMR and UV-Vis spectra. Additionally, NMR and UV-visible spectra suggest the presence of two forms of CQ in solution. A molecular docking study was performed to identify the potency of inhibition of Chloroquine molecule against COVID-19 virus

1. Introduction

For a long time, Chloroquine (CQ) has been recognized because this quinoline derivative was initially used in medicine to treat malaria and because later its use was extended to also treat other diseases such as, light-sensitive skin eruptions, hepatic amoebiasis, lupus erythematosus, rheumatoid arthritis, including the cancer therapy [1-27]. The IUPAC name is 4-*N* -(7-chloroquinolin-4-yl)-1-*N* ,1-*N* -diethylpentane-1,4-diamine. From this year, CQ is used in experimental therapies together with its hydroxychloroquine derivative as potential antiviral agent to treat COVID-19 only in the context of a clinical trial [28]. Many adverse effects appear after long time of using CQ, among which, retinopathy can be mentioned [12,19,23].

So far, there are some studies on the infrared and Raman spectra of CQ but the complete vibrational assignments have not been reported yet [29-32]. Vibrational spectroscopy is not only one of the best tools to identify all species quickly, easily and using a small amount of sample, but it is also used to control the purity of the samples. A study of CQ under physiological conditions by using UV resonance Raman spectroscopy has shown that the rocking CH_2 mode assigned to chloroquine side chain is apparently influenced by protonation of chloroquine [29] while in other study by using surface-enhanced Raman scattering (SERS), CQ was analyzed to recognize substandard and falsified antimalarial drugs present in commercially available tablets [32]. In this context, the structural and vibrational studies of CQ are valuable to characterize in complete form its structure and properties and, besides, to understand the connection between the structure and its mechanism of action. Particularly, structural studies are important to determine which the most stable structure is and, in this way, to produce the complete assignments of all the normal modes of vibration of the compound. Hence, the objectives of this work are: (i) to perform DFT calculations of CQ in gas

phase and aqueous solution by using the B3LYP/6-311++G** method [33,34] where the calculations in solution were performed by using the IEFPCM and universal solvation methods [35-37], (ii) to calculate atomic charges, bond orders, molecular electrostatic potentials, stabilization energies, solvation energy and, topological properties of CQ in both media, (iii) carry out the complete assignments of the normal modes of vibration to the bands observed in the experimental available IR and Raman spectra by using the scaled mechanical force field (SQMFF) methodology, scaling factors, the corresponding normal internal coordinates and the Molvib program [38-40] and, (iv) to predict reactivities and the behaviour of CQ in both media at the same level of theory by using the frontier orbitals and know descriptors [41-46]. Later, the predicted ^{1}H- and ^{13}C-NMR and ultra-visible spectra were compared with the corresponding available ones while the harmonic force constants were also reported. All properties here predicted were compared with the corresponding reported for other antiviral agents [42-47]. Finally, the antiviral activity of CQ and its therapeutic capacity was evaluated against a set of COVID-19-related proteins using docking calculations because it is a very convenient tool for the examination of biological activity [48-53].

2. Material and methods

That experimental CIF file determined for Chloroquine Bis(dihydrogenphosphate) Dihydrate by X-ray diffraction by Karle and Karle was used as an initial theoretical structure for S(-) form of CQ because it has a chiral C and, for this reason, two enantiomeric S(-) and R(+) forms are expected for this antiviral agent [2]. Then, the R(+) form was modelled with the *GaussView* program [54] and, after that, both species were optimized in gas phase and aqueous solution by using the functional hybrid B3LYP/6-311++G** level of theory with the Revision A.02 of Gaussian 09 program [55]. Universal solvation and IEFPCM methods consider the solvent effects and, they were used to optimize the two forms in aqueous solution [35-37,56-58]. The variations of volumes that both forms experiment in solution were computed at the same level of theory with the Moldraw program [59]. The NBO and AIM 2000 programs were used together with the Merz-Kollman charges to calculate atomic charges, molecular electrostatic potentials, acceptors-donors energies and topological properties [60-63]. On the other hand, the ultraviolet-visible spectra for both forms in aqueous solution were predicted with the time-dependent DFT calculations (TD-DFT) while the ^{1}H and NMR chemical shifts for the two enantiomeric forms were calculated with the GIAO in the same medium [64]. The vibrational analyses were performed with the scaled mechanical force field (SQMFF) methodology, the normal internal coordinates, transferable scaling factors and the Molvib program [38-40]. To perform the vibrational assignments potential energy distribution (PED) contributions [?] 10 % were used while the predicted Raman spectra in activities of both forms were corrected to intensities with equations reported in the literature [65,66]. In addition, the gap values were computed as the differences between HOMO and LUMO energies while widely- known equations were used to calculated the chemical potential (μ), electronegativity (χ), global hardness (η), global softness (S), global electrophilicity index (ω) and global nucleophilicity index (E) descriptors [42-47]. The experimental available infrared, ^{1}H and NMR and ultraviolet-visible spectra of CQ were taken of those previously reported in the literature [1]. The calculated properties for the two enantiomeric S(-) and R(+) forms of CQ were compared with those reported for other antiviral agents [42-47]. In addition, the Hirshfeld surfaces (3D) and fingerprint plots (2D) were performed for the S(-) form of CQ to a complete structural description with Crystal Explorer 3.1 software [67] imported on CIF files. Finally, the different structures of COVID-19 enzyme (codes: 6M03 [68], 5R7Y [69], 6W63 [70], 5R81 [71] and 5R84 [72]) are exported from Protein Data Bank of the Structural Bioinformatics Research Laboratory (RCSB) [73]. The preparation of these enzymes for docking calculations was made using Discovery Studio program [74] . Molecular docking analysis was performed by using iGEMDOCK software [75] through the generic evolutionary method (GA) and an empirical scoring function, with the following setting: population size is 800, number 10 of generations is 80 and number of solutions is 10. Intermolecular interactions between COVID-19 protein and Chloroquine for the best docked states have been visualized in Discovery Studio program.

3. Results and Discussion

3.1. Optimizations in both media

The optimized theoretical structures of two enantiomeric S(-) and R(+) forms of CQ are shown in **Figure 1** together with the atoms labelling and the identification of two rings.

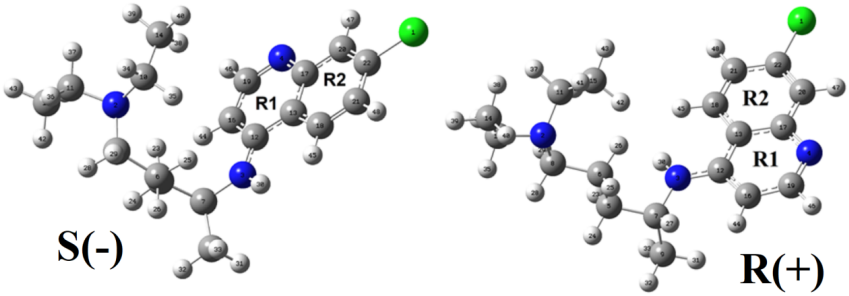

Figure 1. Theoretical structures of free two enantiomeric S(-) and R(+) forms of CQ.

In **Table 1** the properties calculated for the two enantiomeric S(-) and R(+) forms of CQ in both media can be seen by using both hybrid B3LYP/6-311++G** method. Hence, the total energy corrected and uncorrected by ZPVE is presented together with dipolar moment and volume values. The results show that the S(-) form is most stable in gas phase while the R(+) form in aqueous solution. The differences in the energy values in gas phase and aqueous solution are 1.83 and 3.67 kJ/mol, respectively.

Table 1. Calculated total energies (*E*), dipole moments (μ) and volumes (V) of S(-) and R(+) forms of chloroquine in gas phase and aqueous solution by using the B3LYP/6-311++G** Method.

B3LYP/6-311++G** Method	B3LYP/6-311++G** Method	B3LYP/6-311++G** Method	B3LYP/6-311++G** Met
Medium	E (Hartrees)	E_{ZPVE} (Hartrees)	μ (D)
S(-)	S(-)	S(-)	S(-)
GAS	-1326.2932	-1325.8805	6.29
PCM	-1326.1075	-1325.8967	10.13
R(+)	R(+)	R(+)	R(+)
GAS	-1326.2925	-1325.8798	6.24
PCM	-1326.3116	-1325.8981	9.95

Z.P.V.E, zero point vibrational energy

Probably, the higher dipole moment values in the different media justify those results. When the dipole moments vectors for both forms in gas phase are represented we observe that not only the magnitudes of both forms are different but also their orientations and directions are different, as it can be seen in **Figure 2** . On the other hand, the R(+) forms in both media present higher volumes despite the fact that the dipole moments present lower values, as compared with the (S-) forms. Perhaps, the different positions of only donor N-H group could justify that S(-) form in solution has a higher dipole moment value than the other one.

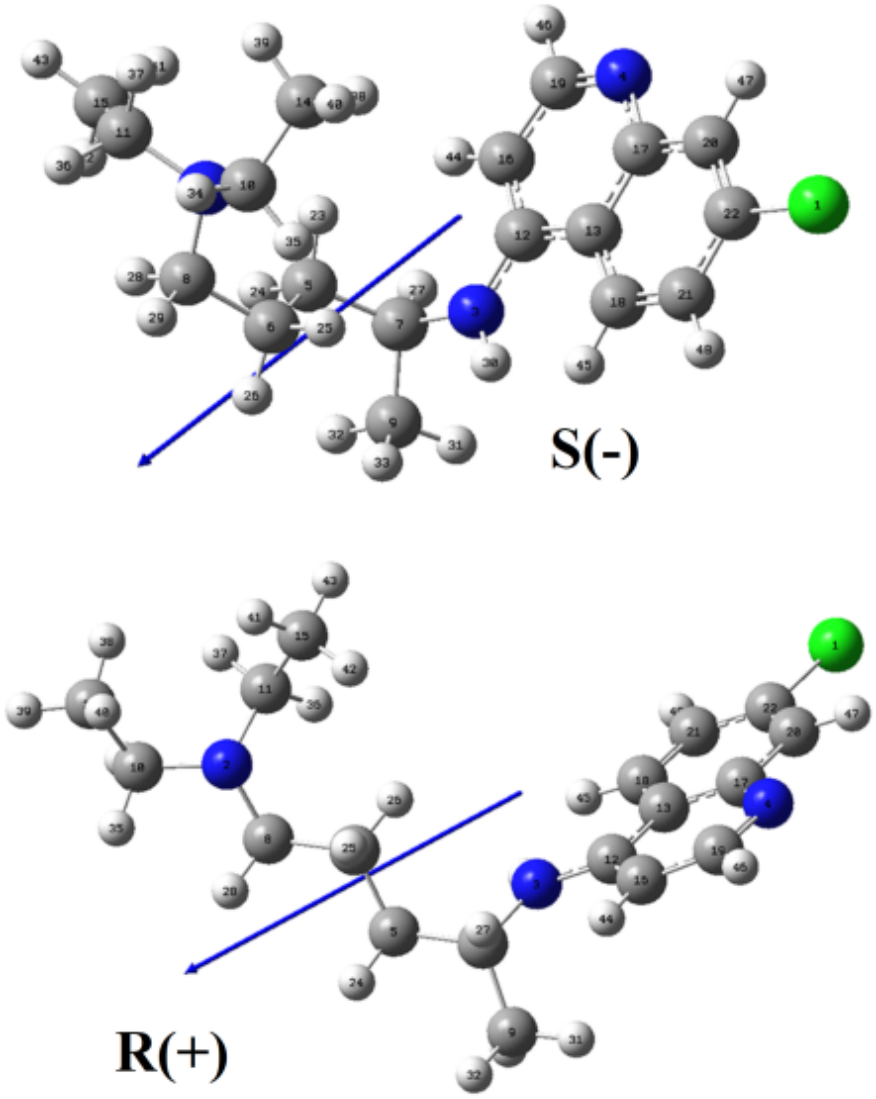

Figure 2 . Magnitudes and positions of vectors of dipole moments of the two enantiomeric S(-) and R(+) forms of CQ in gas phase by using hybrid B3LYP/6-311++G** method.

The differences observed in the dipole moments could have some effect on their properties, especially in aqueous solution. Therefore, the solvation energies are useful parameters highly related to the presence of acceptor and donors H bonds in solution. Hence, for the two enantiomeric S(-) and R(+) forms of CQ the corrected and uncorrected solvation energies by zero point vibrational energy (ZPVE) by using the B3LYP/6-311++G** method are presented in **Table 2** .

Table 2. Corrected and uncorrected solvation energies by zero point vibrational energy (ZPVE) of two enantiomeric S(-) and R(+) forms of CQ by using the B3LYP/6-311++G** method.

Chloroquine[a]	Chloroquine[a]	Chloroquine[a]	Chloroquine[a]
Solvation energy (kJ/mol)	Solvation energy (kJ/mol)	Solvation energy (kJ/mol)	Solvation energy (kJ/mol)

Chloroquine[a]	Chloroquine[a]	Chloroquine[a]	Chloroquine[a]
Species	ΔG_{un} #	ΔG_{ne}	ΔG_c
B3LYP/6-311++G** method	B3LYP/6-311++G** method	B3LYP/6-311++G** method	B3LYP/6-311++G** meth
S(-)	-42.49	12.58	-55.07
R(+)	-48.00	11.91	-59.91

Z.P.V.E, zero point vibrational energy

When these calculated values for CQ are compared with those reported for other antiviral agents by using B3LYP/6-31G* calculations such as, isothiazol (-37,51 kJ/mol) [43], niclosamide (-78,43 kJ/mol) [46], thymidine (-116,16 kJ/mol) [42], cidofovir (-169,21 kJ/mol) and brincidofovir (-227,34 kJ/mol) [45], foscarnet (-219,64 kJ/mol) [44] and amantadine [47], a certain lineal dependence of a ΔG_c is observed with the total acceptor and donors H bonds groups present in their structures, as detailed in **Table 3** .

Table 3 . Corrected solvation energies by ZPVE energies (ΔG_C) and numbers of N-H and O-H groups and N and O atoms present in S(-) and R(+) forms of chloroquine in aqueous solution by using the B3LYP/6-311++G** method. To compared antiviral agents the calculations were performed by using the hybrid B3LYP/6-31G* method.

Species	ΔG_C	N-H	O-H	O	C=O	N	ToTal	Groups	Rings
Amantadine[g]	-20.32	2(NH_2)				1	3	Cl	4 R6
Isothiazol[b,]	-37.51	1				2	3	SH, C[?]N	R5,R6
S(-) CQ[a]	-55.07	1				3	4	Cl	2 R6
R(+) CQ[a]	-59.91	1				3	4	Cl	2 R6
Niclosamide[c]	-78.43	1	1	4	1	2	9	2 Cl, NO_2	2 R6
Thymidine[d]	-116.16	1	2	5	2	2	12	CH_3	R5,R6
Cidofovir[e]	-169.21	2(NH_2)	3	6	1	3	15	H_2PO_3	R6
Foscarnet[f]	-219.64		12	5	2		19	3 Na, PO_3	
Brincidofovir[e]	-227.34	2(NH_2)	2	7	1	3	15	HPO_3	R6

[a]This work, [b]From Ref [43],[c]From Ref [46], [d]From Ref [42], [e]From Ref [45], [f]From Ref [44], [g]From Ref [47].

B3LYP/6-31G* calculations performed for the S(-) form of CQ predict a ΔG_c value of -52.06 kJ/mol [46]. The graphics of total acceptors and donors H bonds groups for antiviral agents versus the ΔG_c values by using B3LYP/6-31G* calculations generate an approximate lineal correlation with a correlation coefficient of $R^2 = 0.8691$ while when the values of both forms of CQ are considered the lineal correlation coefficient increases at $R^2 = 0.9096$. Note that the higher ΔG_c values in the antiviral agents are observed when the total acceptor and donors H bonds groups increase to 19, as it was observed in brincidofovir and in the hydrated foscarnet salt [44,45].

3.2. Geometrical parameters in both media

The optimized geometrical parameters of two enantiomeric S(-) and R(+) forms of CQ in both media were compared in **Table 4** with those experimental corresponding to chloroquine bis(dihydrogenphosphate) dihydrate by X-ray diffraction by Karle and Karle [2]. The correlations are displayed in Table 4 through the values of the root-mean-square deviation (RMSD) values.

Table 4 . Comparison of calculated geometrical parameters for S(-) and R(+) forms of chloroquine in aqueous solution by using the B3LYP/6-311++G** Method compared with the corresponding experimental for Chloroquine Bis(dihydrogenphosphate) Dihydrate by X-ray diffraction by Karle and Karle [2].

B3LYP/6-311++G**	B3LYP/6-311++G**	B3LYP/6-311++G**	B3LYP/6-311++G**	B3LYP/6-311++G**	B3L
Parameters	**S(-)** form[a] Gas	**S(-)** form[a] PCM	**R(+)** form[a] Gas	**R(+)** form[a] PCM	Exp
Bond lengths (Å)	Bond lengths (Å)	Bond lengths (Å)	Bond lengths (Å)	Bond lengths (Å)	Bon
Cl1-C22	1.760	1.767	1.759	1.768	1.75
N2-C8	1.467	1.478	1.462	1.474	1.46
N2-C10	1.469	1.477	1.465	1.474	1.49
N2-C11	1.468	1.477	1.475	1.484	1.55
N3-C7	1.465	1.472	1.465	1.471	1.47
N3-C12	1.366	1.358	1.370	1.353	1.31
N3-H30	1.005	1.009	1.008	1.009	0.76
N4-C17	1.363	1.368	1.363	1.369	1.37
N4-C19	1.317	1.326	1.317	1.326	1.31
C7-C9	1.532	1.529	1.536	1.533	1.50
C7-C5	1.545	1.545	1.536	1.534	1.51
C5-C6	1.532	1.534	1.533	1.533	1.52
C6-C8	1.536	1.535	1.532	1.529	1.54
C10-C14	1.528	1.527	1.528	1.525	1.50
C11- C15	1.528	1.526	1.530	1.527	1.51
C12-C13	1.444	1.448	1.443	1.449	1.44
C12-C16	1.392	1.398	1.392	1.399	1.37
C13-C17	1.429	1.429	1.429	1.428	1.39
C13-C18	1.416	1.416	1.416	1.415	1.38
C16-C19	1.404	1.397	1.405	1.397	1.37
C17-C20	1.419	1.419	1.419	1.419	1.41
C20-C22	1.370	1.371	1.370	1.371	1.35
C21-C22	1.409	1.406	1.409	1.406	1.34
C18-C21	1.376	1.377	1.376	1.377	1.36
C5-H23	1.092	1.093	1.099	1.098	1.07
C5-H24	1.097	1.096	1.095	1.094	1.20
C6-H25	1.095	1.094	1.095	1.096	1.36
C6-H26	1.096	1.095	1.094	1.094	1.05
C7-H27	1.095	1.092	1.094	1.095	0.95
C8-H28	1.093	1.092	1.095	1.094	1.07
C8-H29	1.105	1.104	1.109	1.105	0.99
C9-H31	1.092	1.093	1.092	1.092	0.85
C9-H32	1.092	1.093	1.094	1.094	0.90
C9-H33	1.095	1.094	1.094	1.094	0.90
C10-H34	1.106	1.105	1.107	1.105	1.00
C10-H35	1.092	1.091	1.094	1.093	1.14
C11-H36	1.106	1.105	1.097	1.092	1.03
C11-H37	1.092	1.091	1.097	1.099	1.00
C16-H44	1.081	1.081	1.081	1.081	0.82
C18-H45	1.084	1.083	1.084	1.083	0.93
C19-H46	1.088	1.087	1.088	1.087	0.82
C20-H47	1.082	1.082	1.082	1.082	0.83
C21-H48	1.082	1.082	1.082	1.082	0.81
RMSD	**0.018**	**0.018**	**0.018**	**0.018**	
Bond angles (º)	**Bond angles (º)**	**Bond angles (º)**	**Bond angles (º)**	**Bond angles (º)**	**Bo**
Cl1-C22-C21	118.5	118.5	118.5	118.5	119
Cl1-C22-C20	120.0	119.5	120.0	119.4	119

B3LYP/6-311++G**	B3LYP/6-311++G**	B3LYP/6-311++G**	B3LYP/6-311++G**	B3LYP/6-311++G**	B3L
C20-C17-N4	117.1	117.4	117.1	117.4	115
C17-N4-C19	116.3	116.0	116.3	116.0	113
C12-N3-C7	126.1	125.4	125.4	126.0	125
N3-C7-C9	108.5	108.4	112.0	111.5	110
N3-C7-C5	112.9	112.4	109.1	109.1	110
C9-C7-C5	113.3	113.4	111.7	111.3	112
C7-C5-C6	115.6	115.1	114.4	115.0	114
C5-C6-C8	112.8	114.5	112.3	111.5	113
C6-C8-N2	113.7	115.7	113.4	114.0	112
C8-N2-C10	111.9	109.7	112.5	109.5	113
C8-N2-C11	112.2	109.9	113.4	111.4	108
N2-C10-C14	113.5	114.8	113.3	114.5	112
N2-C11-C15	113.5	114.7	113.6	114.4	111
C10-N2-C11	112.0	109.8	113.2	111.5	111
RMSD	**0.41**	**0.49**	**0.45**	**0.47**	
Diedral angles (º)	**Diedral angles (º)**	**Diedral angles (º)**	**Diedral angles (º)**	**Diedral angles (º)**	**Die**
Cl1-C22-C20-C17	-179.9	179.9	180.0	179.9	-179
C20-C17-N4-C19	-179.9	-179.4	179.9	179.8	-179
C18-C13-C12-N3	-0.8	-3.7	-0.75	-1.2	-2.2
C13-C12-N3-C7	176.7	168.4	172.7	179.6	-178
C16-C12-N3-C7	-4.1	-13.5	-8.9	-0.7	0.5
C12-N3-C7-C9	157.2	159.2	-76.9	-78.9	-150
C12-N3-C7-C5	-76.3	-74.7	158.7	157.8	150
N3-C7-C5-C6	-63.3	-65.5	-66.9	-66.4	61.9
C9-C7-C5-C6	60.5	57.9	168.6	170.1	-174
C7-C5-C6-C8	173.8	177.8	176.6	179.9	175
C5-C6-C8-N2	-64.4	-77.0	176.1	179.5	-73.
C6-C8-N2-C10	-79.5	-76.3	-161.8	-164.4	-85.
C6-C8-N2-C11	153.5	162.9	68.1	71.8	150
C8-N2-C10-C14	155.7	164.6	162.8	171.9	161
C8-N2-C11-C15	-77.5	-75.7	-115.5	-132.7	-81.
C14-C10-N2-C11	-77.3	-74.5	-67.0	-64.4	-75.
C10-N2-C11-C15	155.6	163.6	114.7	104.6	152
RMSD	**34.5**	**40.2**	**45.5**	**45.9**	

[a]This work, [b]From Ref [2]

Very good correlations were found in the bond distances and in the bond angles with RMSD values of 0.018 Å and 0.49-0.41º, respectively while the higher differences originate in the dihedral angles. For the S(-) form of CQ, the RMSD values for dihedral angles is 34.5º while for the R(+) form in both media it slightly increases to 45.9/45.5º. These results indicate that those optimized structures of two forms of CQ can be used to perform the vibrational analysis and to obtain better force fields for both species.

3.3. Charges, molecular electrostatic potential and bond orders studies

Atomic charges, molecular electrostatic potentials and bond orders are interesting properties that can easily explain the behaviour of S(-) and R(+) enantiomers in different media, as it was reported for the two enantiomeric forms of scopolamine alkaloid and antihistaminic promethazine [76,77]. Those two species have also tertiary amine groups as the two forms of CQ, hence, in scopolamine the N atom that belongs to the N-CH_3 group is linked to a ring while in promethazine has a C-N-$(CH_3)_2$ group. But in both species of chloroquine the amine tertiary groups are C-N-$(CH_2$-$CH_3)_2$·groups. Hence, some differences are expected in

these forms of CQ, as compared with those two species. Here, two types of atomic charges for S(-) and R(+) forms of CQ in both media, the Merz-Singh-Kollman (MK) and natural population atomic (NPA) charges were studied by using B3LYP/6-311++G** level of theory. In **Table S1** those calculated charges on all atoms of both enantiomeric forms of CQ can be seen. The behaviour of both charges on the Cl1, N2, N3 and N4 atoms are particularly presented in **Figure 3** .

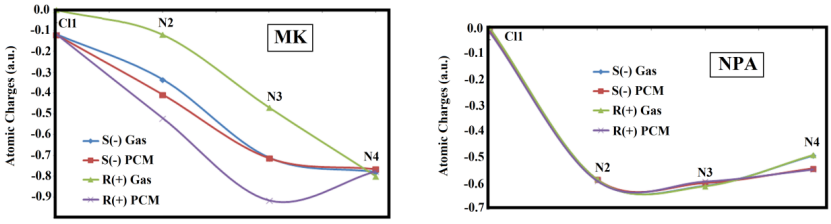

Figure 3. Behaviours of both MK and NPA charges on the Cl1, N2, N3 and N4 atoms of S(-) and R(+) forms of CQ by using B3LYP/6-311++G** level of theory.

Figure 3 shows important differences in the two types of charges analyzed, thus, in the S(-) form, the MK charges on the four atoms studied show the same values (see blue and red lines) with exception of N2 atoms which show mainly negative values in solution while, on the contrary, the MK charges on the four atoms for the R(+) form present different behaviour and values, having these charges in solution the most negative values. Note that the MK charge on N3 atom belonging to N3-H30 bond in solution has the most negative value because the H30 atom is more labile in this medium due to its low value. Moreover, the MK charge on N4 in solution has more negative value than the other ones. Analyzing now the NPA charges (see green and purple lines) similar behaviour on the Cl1, N2 and N3 atoms is observed, however, the NPA charges on the N4 show negative values in solution. As a consequence of these studies, the most negative MK charges values on the four atoms of R(+) form than the S(-) ones could justify their higher stability in solution. The NPA charges on the N4 belonging to ring R1 show the only differences between the two forms in both media.

The molecular electrostatic potentials (MEP) calculated for both forms in the two media from the MK charges [60] show practically the same values and few differences are observed, for this reason they are not presented here. The tendency in the MEP values shows that the MEPs of Cl > N > C > H where clearly higher values are observed in both media on the Cl1 atom while the lower value is observed on the H30 atom because this atom belongs to the N3-H30 bond. When the mapped MEO surfaces 3D for both forms in gas phase by using the *GaussView* program [54] are represented in**Figure S1,** different positions of blue and red colours are observed. Therefore, the strong red colours are observed on the N4 atoms of R1 rings of S(-) and R(+) forms while most weak red colours are observed on the chloroquinolin rings of both forms. Then, strong blue colours can be seen on the N3-H30 bonds because the lowest MEPs are observed on the H30 atoms. Moreover, soft light colours are observed on the other H atoms of aromatic and CH_3 groups, as it is shown in Figure S1. Obviously, the red colours are indicative of nucleophilic sites because there regions are acceptors of H bonds while the blue colours are associated to electrophilic sites because they are donors of H bonds regions, as observed in the donors N3-H30 groups which are strongly donors of H bonds.

Other interesting properties studied here are the bond orders (BO), expressed as Wiberg indexes which have been calculated for the two S(-) and R(+) forms of CQ in both media by using the B3LYP/6-311++G** method. These values for all atoms of both forms are presented in **Table S2** . A very important difference is observed in the BO values of C1, N2 and N4 atoms because the values for these three atoms decrease in solution while the values for the N3 atoms of two forms increase in solution, as it is expected because these atoms belong to N3-H30 bonds which are strongly donors of H bonds in solution. For this latter reason, higher BO values are observed for the N3 atoms of both forms while the lower values in the corresponding H30 atoms.

From these three studies performed in this section, the MK charge and the mapped MEP 3D surfaces have shown significant differences between the S(-) and R(+) species of CQ in both media.

3.4. Stability studies by using NBO and AIM analyses

The presence of donors (N-H) and acceptors (N atoms) H bonds groups in both structures of S(-) and R(+) forms of CQ have revealed different behaviours of MK charges and different mapped MEP 3D surfaces for which, the predictions of their stabilities in the different media are important to explain those differences observed. Besides, different studies have evidenced that acceptors and donors' groups H bonds have a fundamental role in their behaviour as pharmacological drugs [78,79]. For these reasons, in order to investigate intra-molecular or H bonds interactions in both S(-) and R(+) forms of CQ the second order perturbation theory analyses of Fock matrix in NBO Basis were calculated in the two media by using the NBO program [61]. On the other hand, the AIM 2000 program was also employed to compute the topological properties of those two forms of CQ [62,63]. Thus, calculated donor-acceptor interactions of both S(-) and R(+) forms of CQ in the two media by using the B3LYP/6-311++G** method are presented in**Tables S3** and **S4** . Six different σ-ς^* ,π-π^* , n-* , n-* -s^* and π^*-π^* interactions predicted for both forms in gas phase are shown in Table S3·and they clearly favor the R(+) form with a total energy value in gas phase of 9828.18 kJ/mol. However, from Table S4 eight interactions predicted in solution are observed for the two forms which are, σ-ς^* ,σ-π^* , π-ς^* , π-π^* , n-* , n-*, *-*and π^*-π^* interactions where only the σ-ς^* , π-π^* ,n-* , n-*, *-* and π^*-π^* interactions are observed in both forms while the other two σ-π^* and π-ς^*interactions are observed only for the S(-) form in solution. Hence, the total energy value significantly favors the S(-) form of CQ. These results in both media are not in accordance with those calculated from the optimization process because according to Table 1, R(+) is the most stable enantiomer of CQ in solution while S(-) is the most stable form in gas phase. On the contrary, NBO calculations show that R(+) is the most stable enantiomer of CQ in gas phase while S(-) is the most stable form in solution.

With these results different obtained by NBO calculations, it is necessary to investigate intra-molecular or H bonds interactions in both S(-) and R(+) forms of CQ by using the Bader's theory through topological properties. Hence, the electron density, $\rho(\rho)$, the Laplacian values, $[?]^2\rho(\rho)$, the eigenvalues$(\lambda 1, \lambda 2, \lambda 3)$ of the Hessian matrix and, the$|\lambda 1|/\lambda 3$ ratio were calculated for both S(-) and R(+) forms in both media by using the B3LYP/6-311++G** method. The topological properties predicted for the S(-) form of CQ in the two media are observed in **Table S5** while those obtained for the R(+) form in both media are presented in **Table S6** . Table S5 shows three new H bonds interactions for the S(-) form of CQ in gas phase which quickly increase to six in solution. In the molecular graphic presented in **Figure 4** for this form in solution these new C8-H28···H42, N3-H30···H45, C14-H38···C13, C6-H25···H35, C14-H39···H37 and C16-H44···H27 interactions that generate six new RCPs can be seen and which are named from RCPN1 to RCPN6 while RCP1 and RCP2 are the rings of quinolin double-ring structure composed of a chlorobenzene and a pyridine ring. On the contrary, Table S6 shows only two new H bonds interactions for the R(+) form in gas phase while in solution the number increases to three in solution, as it can be observed in the molecular graphic of **Figure 5** .

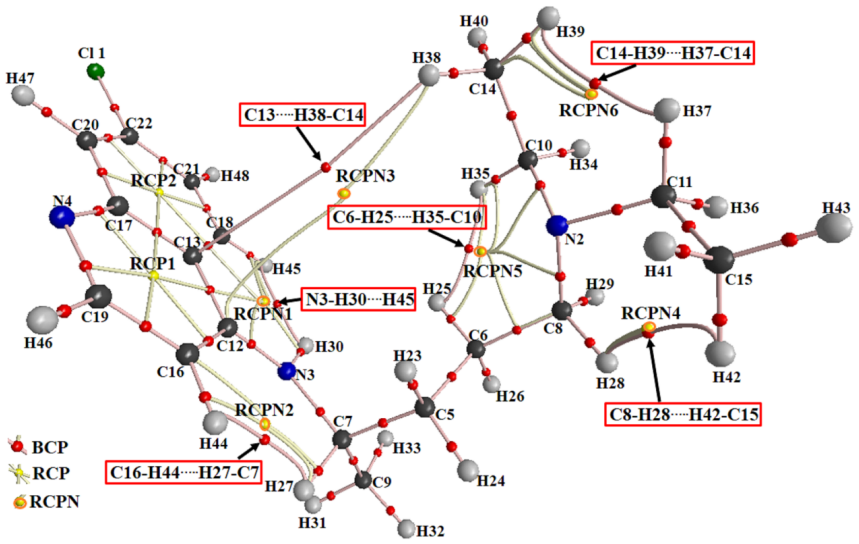

Figure 4. Molecular graphics of S(-) form of CQ in aqueous solution showing their H bonds interactions by using the B3LYP/6-311++G** method.

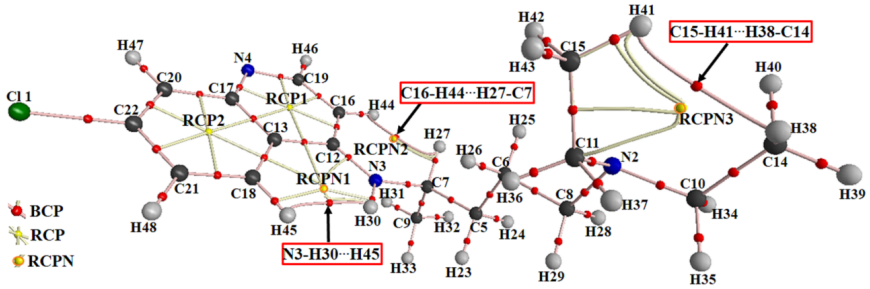

Figure 5. Molecular graphics of R(+) form of CQ in aqueous solution showing their H bonds interactions by using the B3LYP/6-311++G** method.

These three new interactions formed for the R(+) form in solution are: N3-H30···H45, C16-H44···H27 and C15-H41···H38 interactions. Note that the distances between the two atoms involved in the new interactions are the shortest in those interactions produced by the two H30 and H45 atoms of both S(-) and R(+) forms. These analyses reveal that S(-) form of CQ is the most stable in solution than the R(+) one because NBO and AIM calculations have evidenced a higher number of interactions in the S(-) form in this medium than the other one.

3.5. Frontier orbitals and global descriptors studies

Taking into account the widely-known antiviral properties reported for CQ [1-27] and, particularly, its potential use to treat COVID-19 [28] the reactivities and behaviour of both S(-) and R(+) forms in the two media should be investigated. Hence, calculations of frontier orbitals HOMO and LUMO were used to compute the gap values and chemical potential (μ), electronegativity (χ), global hardness (η), global softness (S), global electrophilicity index (ω) and global nucleophilicity index (E) descriptors by using known equations [41-47]. Therefore, the results of those properties for both S(-) and R(+) forms in gas phase are presented in**Table S7** by using the B3LYP/6-311++G** method while the values for these forms of CQ are compared with the corresponding to antiviral isothiazol, thymidine, cidofovir, brincidofovir, foscarnet,

niclosamide and amantadine agents in **Table S8** [42-47]. The structures of all compared antiviral agents are presented in **Figure S2** . The analyses of results for both S(-) and R(+) forms of CQ show that the S(-) forms (4.3729 and 4.2994 eV) in both media are slightly more reactive than the R(+) ones (4.3924 and 4.3021 eV) because there are little differences between the values in gas phase and in aqueous solution. Both forms are more reactive in solution. When those gap values are compared with other antiviral agents from Table S8 brincidofovir (3.7715 eV) and niclosamide (4.2205 eV) they are the more reactive than the other ones. Note that the value for brincidofovir was calculated by using B3LYP/6-31G* method while niclosamide was calculated with the same method than both forms of chloroquine. Hence, it is observed that potential antiviral to COVID-19 niclosamide is better than both forms of chloroquine and, therefore, both forms of CQ could be used to treatment of COVID-19. These differences are justified by the two Cl atoms present in niclosamide in addition to NO_2 group and to the nine acceptors and donors groups different from both forms of CQ because these only have a Cl atom and 4 acceptors and donors groups. In relation to the descriptors, the S(-) form has lower electrophilicity index in gas phase but a higher value in solution than the R(+) one while a same tendency it is observed for the S(-) form in the nucleophilicity index. If now these two electrophilicity and nucleophilicity indexes are compared with the predicted for other antiviral agents we observe that niclosamide presents a higher electrophilicity index value while foscarnet presents the highest nucleophilicity index. The presence of 19 acceptors and donors groups in addition to three Na atoms and phosphate group in foscarnet could justify that high value predicted for the nucleophilicity index.

3.6. Vibrational study

In this analysis, we have considered the two forms of CQ because the energy differences between both forms in gas phase and solution are low (1.83 and 3.67 kJ/mol) and, also due to the fact that in gas phase the S(-) form is the most stable while in aqueous solution the R(+) form is the most stable one. Hybrid B3LYP/6-311++G** calculations have optimized both enantiomers S(-) and R(+) of CQ with C_1symmetries and, as their structures have 53 atoms a total of 153 vibration modes are expected in the experimental spectra. In this case, all vibration modes are active in both infrared and Raman spectra. The experimental available IR spectrum was taken from that reported in the solid phase in KBr pellet [1]. Comparisons of that experimental spectrum with the corresponding theoretical for both forms in gas phase are presented in **Figure 6** while the corresponding predicted Raman spectra can be seen in **Figure 7** . The theoretical Raman spectra predicted in activities were corrected to intensities by using known equations [65,66]. The SQMFF methodology and the Molvib program were used to calculate the harmonic force fields for both forms of CQ in gas phase by using B3LYP/6-311++G** calculations together with transferable scaling factors and the normal internal coordinates [38-40]. In the assignments potential energy distribution (PED) contributions [?] 10 % were used. **Table 5** shows calculated and observed wavenumbers for the S(-) and R(+) forms of CQ in gas phase by using B3LYP/6-311++G** calculations. Both Figures 6 and 7 show clear differences in the intensities of some bands between the S(-) and R(+) forms.

Figure 6. Experimental available Infrared spectra of chloroquine in solid phase [1] compared with the predicted for the S(-

Table 5 . Observed and calculated wavenumbers (cm^{-1}) and assignments for S(-) and R(+) forms of chloroquine in aqueous solution by using the B3LYP/6-311++G** method in gas phase by using B3LYP/6-311++G** calculations.

ATR[a]	B3LYP/6-311++G**[a]	B3LYP/6-311++G**[a]	B3LYP/6-311++G**[a]	B3LYP/6-311++G**[a]
	S(-) Form	S(-) Form	R(+) Form	R(+) Form
	SQM[d]	Assignments[a]	SQM[d]	Assignments[a]
3461vw	3505	νN3-H30	3476	νN3-H30
3257w	3080	νC20-H47	3079	νC20-H47
3110w	3076	νC16-H44	3075	νC16-H44
3083w	3071	νC21-H48	3072	νC21-H48

ATR[a]	B3LYP/6-311++G**[a]	B3LYP/6-311++G**[a]	B3LYP/6-311++G**[a]	B3LYP/6-311++G**[a]
3025w	3032	νC18-H45	3039	νC18-H45
	3002	νC19-H46	3002	νC19-H46
2979m	2977	ν_aCH$_3$(C9)	2976	ν_aCH$_3$(C9)
	2976	ν_aCH$_3$(C14)	2976	ν_aCH$_3$(C15)
	2972	ν_sCH$_3$(C9)	2972	ν_aCH$_3$(C14)
	2964	ν_aCH$_3$(C14)	2963	ν_aCH$_3$(C14)
	2962	ν_aCH$_3$(C9)	2961	ν_aCH$_3$(C9)
	2962	ν_aCH$_3$(C9)	2961	ν_aCH$_3$(C15)
	2957	ν_aCH$_2$(C5)	2949	ν_aCH$_2$(C6)
	2944	ν_aCH$_2$(C11)	2926	ν_aCH$_2$(C10)
	2942	ν_aCH$_2$(C8)	2920	ν_aCH$_2$(C5)
2936m	2937	ν_aCH$_2$(C10)	2913	νC7-H27
2925sh	2922	ν_aCH$_2$(C6)	2911	ν_aCH$_2$(C8)
	2905	ν_sCH$_3$(C14)	2904	ν_sCH$_3$(C14)
	2904	ν_sCH$_3$(C9)	2903	ν_sCH$_2$(C6)
	2902	ν_sCH$_3$(C15)	2900	ν_sCH$_3$(C15)
2870w	2899	νC7-H27	2899	ν_sCH$_3$(C9)
	2894	ν_sCH$_2$(C6)	2898	ν_aCH$_2$(C11)
2805w	2884	ν_sCH$_2$(C5)	2869	ν_sCH$_2$(C11)
2790sh	2795	ν_sCH$_2$(C8)	2866	ν_sCH$_2$(C5)
2751sh	2785	ν_sCH$_2$(C10)	2772	ν_sCH$_2$(C10)
2728sh	2782	ν_sCH$_2$(C11)	2755	ν_sCH$_2$(C8)
1611m	1590	νC20-C22,νC13-C18	1590	νC20-C22,νC13-C18
1586s	1567	νC12-C16,νC18-C21	1568	νC12-C16,νN4-C19
1573vs	1553	νC16-C19	1553	νC16-C19
1545s	1512	βN3-H30,νN3-C12	1511	βN3-H30,νN3-C12
1489m	1465	βN3-H30,νC21-C22	1466	βN3-H30,νC21-C22
1466sh	1455	δCH$_2$(C11), δCH$_2$(C10)	1460	δCH$_2$(C10),δCH$_2$(C8)
1459sh	1447	δ_aCH$_3$(C14)	1450	δCH$_2$(C11)
1452s	1441	δCH$_2$(C8)	1445	δCH$_2$(C6)
1443sh	1440	δ_aCH$_3$(C9) δCH$_2$(C5)	1437	δ_aCH$_3$(C14)
1439sh	1437	δ_aCH$_3$(C14) δ_aCH$_3$(C14)	1436	δ_aCH$_3$(C9)
	1435	δ_aCH$_3$(C9)	1432	δ_aCH$_3$(C15)
	1432	δ_aCH$_3$(C15)	1431	δ_aCH$_3$(C9)
1430sh	1430	βC19-H46	1430	βC19-H46
1425m	1428	δCH$_2$(C10)	1425	δ_aCH$_3$(C15)
	1424	δ_aCH$_3$(C14),δ_aCH$_3$(C15)	1422	δCH$_2$(C8)
	1422	δCH$_2$(C11)	1421	δCH$_2$(C10),δ_aCH$_3$(C14)
1418sh	1418	δCH$_2$(C6), δCH$_2$(C5)	1420	δCH$_2$(C5)
1391sh	1405	νC12-C13	1408	wagCH$_2$(C8)
	1392	wagCH$_2$(C8),ρCH$_2$(C5)	1403	βC16-H44,νC12-C13
	1386	wagCH$_2$(C10)	1377	ρCH$_2$(C5)
1378m	1383	wagCH$_2$(C11)	1371	wagCH$_2$(C11)
	1378	wagCH$_2$(C10) ρCH$_2$(C5)	1364	wagCH$_2$(C10)
1378m	1363	νC17-C20	1363	νC17-C20
1362sh	1352	δ_sCH$_3$(C9)	1349	δ_sCH$_3$(C9)
	1347	δ_sCH$_3$(C14)	1347	δ_sCH$_3$(C15)
1342sh	1344	δ_sCH$_3$(C15)	1343	δ_sCH$_3$(C14)
	1339	ρ'C7-H27,C13-C17	1342	δ_sCH$_3$(C14) δ_sCH$_3$(C15)
1337sh	1333	ρC7-H27,wagCH$_2$(C6)	1326	ρ'C7-H27

ATR[a]	B3LYP/6-311++G**[a]	B3LYP/6-311++G**[a]	B3LYP/6-311++G**[a]	B3LYP/6-311++G**[a]
	1326	ρ'C7-H27	1322	ρC7-H27
	1307	νC13-C17	1312	ρCH_2(C11)
1332m	1303	ρCH_2(C8)	1310	νC13-C17
	1302	ρCH_2(C11)	1304	ρCH_2(C8), ρCH_2(C10)
1294sh	1293	ρCH_2(C10)	1282	ρCH_2(C6)
1282w	1284	wagCH_2(C5)	1271	wagCH_2(C5)
1258m	1262	νN4-C19	1264	wagCH_2(C6)
1246sh	1250	ρCH_2(C8)	1257	νN4-C19
1219w	1235	βC18-H45	1235	βC18-H45
1197w	1209	ρCH_2(C6)	1198	ρCH_2(C6),wagCH_2(C5)
1179vw	1186	νN4-C17	1178	νN2-C8,νN2-C11
1165m	1173	νN2-C8	1177	νN4-C17
1154m	1162	βC21-H48	1161	βC21-H48,νC18-C21
	1145	νN3-C7	1150	βC21-H48,νN2-C10
1133m	1130	νN2-C10	1124	νC7-C5,νN3-C7
	1107	βR_1(A2),βC16-H44	1117	βR_1(A2)
	1099	ρCH_3(C9)	1097	ρ'CH_3(C9)
	1080	ρCH_3(C9)	1080	ρCH_3(C15),ρCH_3(C14)
1083m	1059	ρCH_3(C15)	1067	ρCH_3(C15), νC7-C9
1067sh	1057	νC7-C9	1064	ρCH_3(C14),ρCH_3(C15)
1056sh	1052	βC20-H47	1053	νC21-C22,βC20-H47
	1046	ρCH_3(C14)	1043	ρ'CH_3(C14)νC10-C14,νN2-C8
1036w	1041	νC6-C8,νN2-C8	1038	ρ'CH_3(C15)
1022w	1031	νC16-C19	1033	νN2-C10
986w	999	νC6-C8	1014	νC6-C8
982sh	971	νC5-C6	997	νC5-C6,νC7-C9
	968	γC20-H47	968	γC20-H47
956w	964	νC10-C14	967	νC11-C15
	942	ρ'CH_3(C9)	959	τwCH_2(C8), τwCH_2(C6)
936sh	935	γN3-H30	937	γN3-H30
932w	897	νC11-C15	929	ρCH_3(C9)
905w	893	γC21-H48	899	νC11-C15, ρ'CH_3(C14)
884sh	887	βR_1(A2)	894	γC21-H48
877m	881	τwCH_2(C5)	888	βR_1(A2)
853m	858	βR_1(A1)	858	βR_1(A1), βR_2(A1)
842sh	836	βR_1(A1)	838	ρ'CH_3(C9)
823w	814	γC18-H45	815	γC18-H45
799m	797	γC19-H46	798	γC19-H46
771w	775	νC7-C5,τwCH_2(C8)	785	τwCH_2(C8)
762sh	766	τwCH_2(C5) τwCH_2(C10)	765	τwCH_2(C10)
	749	τR_1(A1)	751	τR_1(A1)
	747	τwCH_2(C11) ρ'CH_3(C15)	746	νC13-C17
	745	νC13-C17	739	νN2-C11
717w	733	τwCH_2(C10)	720	τwCH_2(C11)
674vw	680	τwCH_2(C6)	678	τwCH_2(C6),τwCH_2(C5)
648w	656	βR_3(A2),βR_2(A2)	657	βR_3(A2),βR_2(A2)
	638	τR_1(A2)	637	τR_1(A2)
622w	620	τR_2(A1), τR_1(A2)	621	τR_2(A1)
599w	608	δC5C7N3,δC5C7C9 δC7C5C6	595	βR_3(A1),νC22-Cl1
549w	593	βR_3(A1), νC22-Cl1	545	δC14C10N2,βR_3(A2)

ATR[a]	B3LYP/6-311++G**[a]	B3LYP/6-311++G**[a]	B3LYP/6-311++G**[a]	B3LYP/6-311++G**[a]
	528	βR_2(A1)	528	δC6C8N2
	505	βC12-N3	514	δC9C7N3
500m	499	τR_3(A1),γC22-Cl1	501	τR_3(A1),γC22-Cl1
489sh	476	δC6C8N2	494	βC12-N3
461sh	468	δC14C10N2	451	δC9C7N3,δC15C11N2
	439	δC15C11N2	429	τR_2(A2)
	426	τR_2(A2),ButtC17-C13	424	δC5C7C9
422w	416	τR_2(A2), δC5C7C9	413	δC5C7N3
402w	378	δC9C7N3	400	γC16-H44
	347	δC8C6C5	363	δC8N2C11
361vw	327	δC9C7N3, δC8N2C10	352	γC16-H44
	306	δC11N2C10 δC8N2C11	335	δC14C10N2
312sh	286	δC14C10N2	301	γC16-H44,δC6C8N2
277sh	276	τR_2(A2), γC22-Cl1	272	ButtC17-C13
	252	γC16-H44	250	τR_3(A1)
	246	τR_2(A1)	240	$\tau_w CH_3$(C14)
248sh	241	βC22-Cl1	237	τR_2(A1), τR_3(A1)
	232	$\tau_w CH_3$(C9), δC8C6C5	226	$\tau_w CH_3$(C9)
234sh	220	$\tau_w CH_3$(C9)	221	δC8C6C5
210sh	209	$\tau_w CH_3$(C9)	208	$\tau_w CH_3$(C9), βC22-Cl1 δC12N3
210sh	199	$\tau_w CH_3$(C14) $\tau_w CH_3$(C15)	198	$\tau_w CH_3$(C15)
193vs	196	$\tau_w CH_3$(C14) $\tau_w CH_3$(C15)	173	δC7C5C6, δC8N2C10
	176	δC7C5C6	146	τN2-C8
	129	τC5-C7	137	τC5-C7,τC8-C6
	112	τC8-C6	120	τR_2(A2),τR_2(A1)
	108	δC12N3C7,βC12-N3	111	τC10-N2
	92	τN3-C12,τC10-N2	89	τN3-C12, R_3(A2)
	82	τC11-N2	88	τC5-C7, δC8C6C5
	70	τC10-N2, τR_3(A2)	65	τR_3(A2)
	54	τN2-C8	46	τN3-C12,τC8-C6
	35	τN2-C8,τN2-C8	45	τC11-N2,τC10-N2
	25	τC6-C5	22	τC7-N3
	15	τC7-N3	19	τC6-C5,τC11-N2
	6	τN3-C12,τC7-N3	14	τN3-C12

Abbreviations: ν, stretching; β, deformation in the plane; γ, deformation out of plane; τ, torsion; β_R. deformation ring τ_R, torsion ring; ρ, rocking; τw, twisting; δ, deformation; a, antisymmetric; s, symmetric; (A_1), Ring 1; (A_2), Ring 2; [a]This work,[b]From scaled quantum mechanics force field.

Particularly, in the IR spectrum of R(+) form in the 2000-400 cm^{-1} region bands with higher intensities are observed while in the higher wavenumbers region the observed IR bands are wide due to the packing forces not considered in the calculations in gas phase. Predicted Raman spectra for both forms show higher differences in the 900-100 cm^{-1} region evidencing higher intensities some bands of S(-) form, as observed in Figure 7. Discussions of assignments of more important groups are presented below by regions.

3.6.1. Band Assignments

4000-2000 cm^{-1} region . In this region, typical bands corresponding to stretching modes of CH_2, CH_3, N-H and C-H groups of S(-) and R(+) forms of CQ are expected [42-47,51-53,76,77]. The observed weak band at 3461 cm^{-1} can be assigned to the N3-H30 stretching modes of both forms while the group of IR bands located between 3257 and 3025 cm^{-1} are attributed to aromatic C-H stretching modes of both fused

rings. The only aliphatic C3-H27 bonds corresponding to chiral C7 atom of both forms are predicted by SQM calculations in different positions, thus, in the S(-) form this modes is assigned to the weak band at 2870 cm^{-1} because it is predicted at 2899 cm^{-1}. In the R(+) form that stretching mode is predicted at 2913 cm^{-1} and assigned to the IR of medium intensity at 2936 cm^{-1}. Due to the presence of five CH_2 groups in both forms of CQ, a total of ten anti-symmetric and symmetric stretching modes are expected for the two species, hence, these modes are predicted between 2957 and 2755 cm^{-1} and assigned to observed IR bands in this region. On the other hand, nine anti-symmetric and symmetric stretching modes are expected for both forms due to the three CH_3 groups; therefore, they are assigned as predicted by calculations between 2977 and 2900 cm^{-1}. The symmetries of $CH_2$and CH_3 modes were no confirmed due to the absence of a Raman spectrum.

1800-1000 cm^{-1} region . In this region, the C-C and C-N stretching modes together with deformation, wagging and rocking modes of CH_2, CH_3 and aromatic and aliphatic C-H groups are expected [42-47,51-53,76,77]. Here, the N4=C19 stretching mode in the R(+) forms is predicted to 1568 cm^{-1} with double bond character while in the S(-) form as partial double bond character at 1262 cm^{-1}, hence, they are assigned to the strong and medium intensity bands at 1586 and 1258 cm^{-1}, respectively. Also, in the R(+) form that modes is predicted with higher PED contribution at 1257 cm^{-1}. The C=C stretching modes of both forms are assigned to the very strong, strong and medium intensities IR bands between 1611 and 1489 cm^{-1}, as observed in similar compounds and as detailed in Table 5 [42-47,51-53,76,77]. The CH_2 deformations modes are normally found in the 1485-1410 cm^{-1} region [42-47,51-53,76,77]. In both forms of CQ, the SQM calculations predict these modes between 1450 and 1420 cm^{-1}, hence, these vibration modes are assigned to the IR bands observed in this region. The two anti-symmetric and symmetric CH_3 deformation modes are assigned as predicted by calculations between 1440 and 1342 cm^{-1}. The wagging and rocking CH_2 modes in both forms are predicted between 1408/1198 and 1392/1209 cm^{-1} while the rocking CH_3 modes in the 1099 and 838 cm^{-1} region. Hence, those vibration modes are assigned in the regions predicted by SQM calculations. On the other hand, the aromatic βC-H rocking modes are predicted by SQM calculations in the two forms between 1403 and 1053 cm^{-1}, as in similar species and, for these reasons, they are assigned in that region [42-47,51-53,76,77].

1000-40 cm^{-1} region. The $CH_2$and CH_3 twisting modes are expected in this region together with C-C and N-C stretching and out-of-plane C-H deformation modes and other different skeletal modes [42-47,51-53,76,77]. In both forms, the CH_2 and CH_3 twisting modes are assigned as predicted by SQM calculations to the bands observed between 959/678 and 232/196 cm^{-1}, respectively [42-47,51-53,76,77]. The deformations and torsions rings are predicted from 1117 up to 65 cm^{-1}. Then, the assignments of other vibration modes are specified in Table 5.

3.7. Force constants

The harmonic force fields for the S(-) and R(+) forms of CQ in both media, calculated with the SQMFF method and the Molvib program by using the B3LYP/6-311++G** level of theory, were used to obtain the corresponding scaled force constants [38-40]. Hence, the scaled force constants for some groups of both forms of CQ are summarized in**Table 6** compared with those reported in gas phase for the two hydrochloride forms of antihistaminic promethazine agent by using the B3LYP/6-31G* method [77]. First, regarding the scaled force constants for the S(-) and R(+) forms of CQ in both media we observed that the $\varphi(\nu N\text{-}H)$,$\varphi(\nu N\text{-}(^{\sim}H_2\text{-}^{\sim}H_3)_2$ and $\varphi(\nu^{\sim}\text{-}N)_P$ force constants present slight differences in both media, being their values lower in solution. These lower values for both forms are related to the enlargement of involved N3-H30, N2-C10, N2-C11, N4-C19 and N4-C17 bonds. The N3-H30 bonds are donors of H bonds and, as a consequence they are hydrated in solution while the N2 atoms are acceptors of H bonds increasing the N2-C10 and N2-C11 distances in solution, as observed in Table 3.

Table 6 . Scaled internal force constants for S(-) and R(+) forms of chloroquine in gas phase and aqueous solution by using the B3LYP/6-311++G** method.

Force constant	B3LYP/6-311++G** method	B3LYP/6-311++G** method	B3LYP/6-311++G** method	B3LYP/
	Chloroquine	Chloroquine	Chloroquine	Chloroq
	S(-)	S(-)	R(+)	R(+)
	Gas	PCM	Gas	PCM
$\varphi(\nu N\text{-}H)$	6.82	6.69	6.71	6.69
$\varphi(\nu N\text{-}(\tilde{\nu}H_2\text{-}\tilde{\nu}H_3)_2$	4.46	4.39	4.47	4.34
$\varphi(\nu\tilde{\ }\text{-}N)_P$	7.02	6.74	7.04	6.75
$\varphi(\nu\tilde{\ }\text{-}N)$	5.47	5.40	5.40	5.55
$\varphi(\nu\tilde{\ }H_2)$	4.60	4.63	4.57	4.62
$\varphi(\nu\tilde{\ }H_3)$	4.79	4.79	4.79	4.78
$\varphi(\nu\tilde{\ }\text{-}H)_P$	5.11	5.14	5.12	5.15
$\varphi(\nu\tilde{\ }\text{-}H)$	4.64	4.77	4.69	4.68
$\varphi(\nu\tilde{\ }{=}\tilde{\ })$	6.16	6.17	6.17	6.18
$\varphi(\nu\tilde{\ }\text{-}\tilde{\ })$	4.00	4.08	3.97	4.07
$\varphi(\delta\tilde{\ }H_2)$	0.77	0.77	0.77	0.76
$\varphi(\delta\tilde{\ }H_3)$	0.53	0.52	0.53	0.52

Units are mdyn Å^{-1} for stretching and mdyn Å rad^{-2} for angle deformations

[a]This work, [b]From Ref [77] for promethazine**.**

On the other hand, the $\varphi(\nu\tilde{\ }\text{-}N)_P$ force constants also present lower values in solution due to the fact that the involved N4-C19 and N4-C17 bonds belong to N4 atoms of pyridine rings and, hence, these are also acceptors of H bonds. The other scaled force constants in both species practically present the same values. If now the constants are compared with the reported for both forms of promethazine, we observed important differences in the scaled $\varphi(\nu N\text{-}H)$ and$\varphi(\nu N\text{-}\tilde{\nu}H_3)$ force constants. The low values observed in both forms of hydrochloride promethazine can be attributed to the ionic N-H··· Cl bonds because the electronegativity of Cl atoms produces a strong enlargement of N-H bonds diminishing the values while the low value in the $\varphi(\nu N\text{-}\tilde{\nu}H_3)$ is related to the different groups linked to tertiary N atoms acceptors of H bonds. In CQ, the tertiary N2 atoms are linked to two CH_2-CH_3 groups while in promethazine the tertiary N atoms are linked to two CH_3 groups.

3.8. NMR study

For both S(-) and R(+) forms of CQ the ^{1}H and NMR chemical shifts were predicted in aqueous solution by using the GIAO and hybrid B3LYP/6-311++G** methods [64]. Comparisons of those values with the corresponding experimental ones taken from Ref [1] for CQ in $CDCl_3$ and DMSO**-** $_{d6}$ are presented through RMSD values in **Tables S9** and**10** . Very good correlations are observed in the RMSD values of both ^{1}H and nucleus (0.14- 0.08 ppm for^{1}H and 1.65-1.23 ppm for ^{13}C) which could suggest the presence of both forms in solution because there are not significant differences in both media between the S(-) and R(+) forms of CQ.

3.9. Electronic spectrum

The ultraviolet-visible spectra of S(-) and R(+) forms of CQ were predicted in aqueous solution with the time-dependent DFT calculations (TD-DFT) and they are compared in **Figure 8** with the corresponding experimental in methanol solution taken from Ref [1]. The same curves obtained for the two S(-) and R(‘+) forms could indicate the presence of both enantiomers in solution, in accordance to the experimental UV-Vis spectrum and to the ^{1}H- and^{13}C-NMR studies. In the experimental UV-Vis spectrum recorded between 200 to 400 nm are observed maxima at 218, 253 and 328 nm and minima at 243 and 275 nm while the predicted visible absorption wavelengths and oscillator strength (f) for both enantiomers of chloroquine can be observed in **Table S11** . The positions of these bands are in agreement with those observed in other quinoline compounds [80]. The different bands observed in the experimental spectrum can be associated to the different transitions predicted by NBO calculations in aqueous solution, as detailed in Table S4.

The different observed bands can be assigned to n-* , π-π^* , n-*and σ-ς^* transitions predicted by NBO calculations with higher energy values.

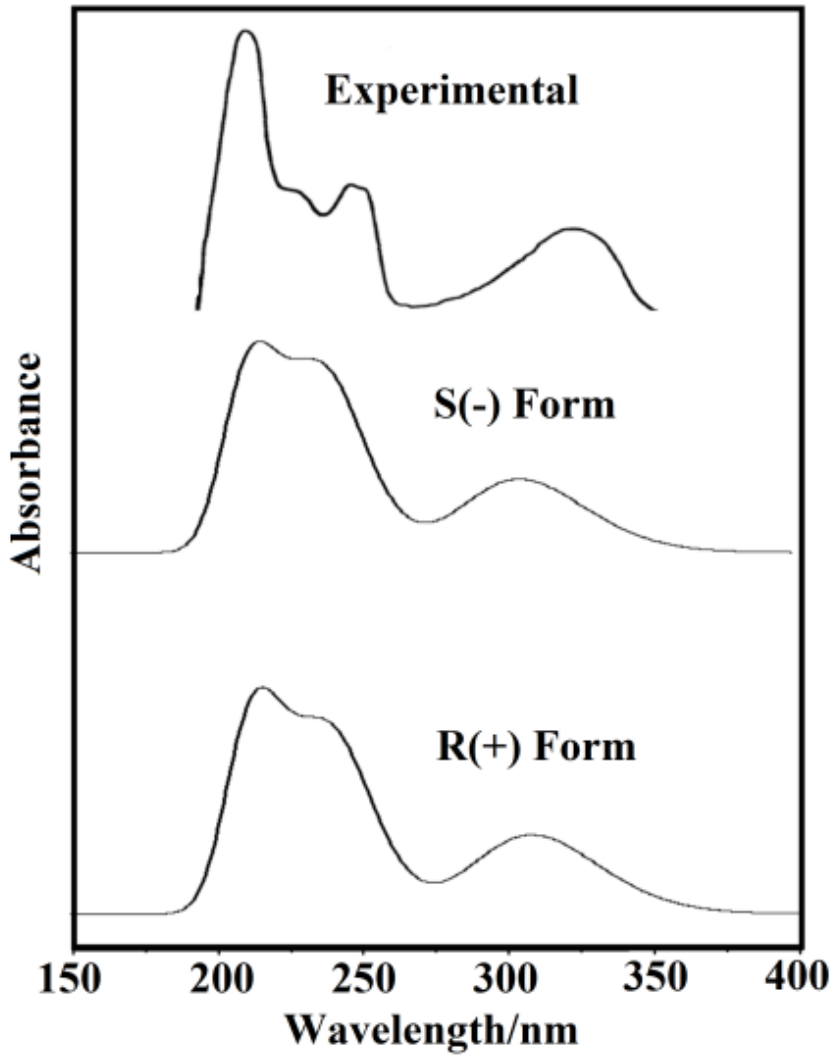

Figure 9 . Experimental available spectrum of hydrochloride amantadine in aqueous solution [6] compared with those predicted for the three species in the same medium by using the B3LYP/6-311++G** method.

3.10. Hirshfeld surface investigation

The Hirshfeld surfaces analysis (3D) and fingerprint plots (2D) are two necessary approaches to evaluate and complete the structural description, both were carried out with Crystal Explorer 3.1 software [67] imported on CIF files. 3D graphics provide a three-dimensional image of intermolecular and intramolecular interactions in crystals, while two-dimensional plots obtained by Hirshfeld surface analysis can identify each type of intermolecular interaction, they are based on the d_e and d_i distances to identify the nature of contacts where the term $d_e$corresponds to the distance separating the Hirshfeld surface and the nearest atomic nucleus located outside on this surface. As for the term d_i , it corresponds to the distance separating the Hirshfeld surface from the nearest atomic nucleus located inside the surface. These two terms are connected with the van der Waals rays by the normalized distance (d_{norm}) according to the following equation:

$$d_{\text{norm}} = \frac{d_i - r_i^{\text{vdW}}}{r_i^{\text{vdW}}} + \frac{d_e - r_e^{\text{vdW}}}{r_e^{\text{vdW}}}$$

Chloroquin molecular Hirshfeld surfaces were generated using standard high resolution. The d_{norm} surface (Fig. 10a) is mapped on a color scale varying from -0.388 to 1.402, the *ShapeIndex* graph (Fig. 10b) located in the color range of -1.0 - 1.0 and *Curvedness* in the range of -4.0 to 4.0 (Fig. 10c).

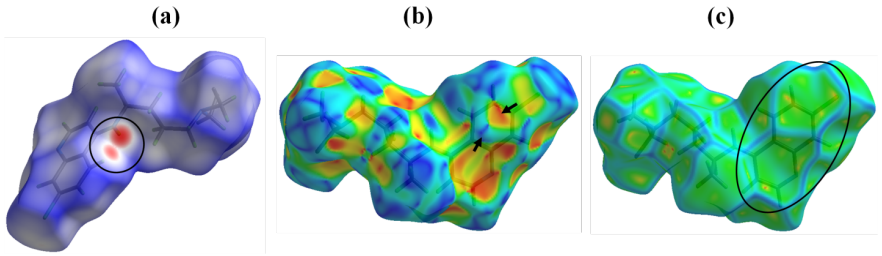

Fig. 10. Hirshfeld surfaces "d_{norm} ", "*Shape index* " and "*Curvedness* " of Chloroquine molecule.

The normalized contact distance (d_{norm}) of the Chloroquin compound makes it possible to graphically illustrate the relative positioning of the neighboring atoms belonging to the molecule interacting together. This analysis type displays a surface with a color scheme (red, blue, white), where the red spots highlight the shortest intermolecular contacts which are attributed to C-H···N interactions. The blue areas indicate the most language intermolecular contacts in the structure and the white regions represent the contacts around the van der Waals separation. The latter corresponds respectively to the H···H, C···H and H···Cl interactions [81-84]. Concerning the two maps (3D) Shape index and Curvedness, indeed the two blue and red triangles located at the level of Chloroquin phenyl on the Shape index cartography and the large flat region delimited by a blue outline observed on the Curvedness graph suggest the presence of C-H... π interactions [83]. The percentages of the different contacts as well as the fingerprint plots of the main contacts existing in the chloroquin structure are illustrated respectively in Figs. 11 and 12. The hydrogen-hydrogen contacts (H ... H) (Fig. 12a) occupy almost half of the entire Hirshfeld surface (44.6%) with a high concentration in the central region where $d_e = d_i$ = 1.1Å. C... H / H... C (Fig. 12b) and H... Cl / Cl... H (Fig. 12c) contacts comprise respectively 29.8% and 10.2% of the entire Hirshfeld surface and represented by two symmetrical wings with $d_e + d_i$ ~ 3 Å and 3.2 Å, the large percentage (29.8%) confirms the presence of the C-H... π interactions already mentioned in the three-dimensional graphs (Shape index and Curvedness). The nitrogen-hydrogen contacts (N... H / H... N) show on its 2D graph the presence of two narrow and symmetrical pointed points centered around a sum $d_e + d_i$ ~ 2.2 Å, these contacts are responsible for the hydrogen bonds C-H... N. Based on the van der Waals rays of involved atoms in contacts (H: 1.09 Å, C: 1.70 Å, N: 1.55 Å, Cl: 1.75) Å and the d_e and d_i distances we carried out a comparative study to find out the nature of contacts, close or distant, this study is summarized in Table 7. We note from this table that only N... H / H... N contacts are considered close with a sum $d_i + d_e$ less than the sum of van der Waals rays of involved atoms.

Table 7 Nature of main contacts existing in chloroquine molecule.

Contacts	$d_i + d_e$ (Å)	Σ RVW (Å)	Contacts nature
H...H	2.2	2.18	Distant
C...H/H...C	3	2.79	Distant
H...Cl/Cl...H	3.2	2.84	Distant
N...H/H...N	2.2	2.64	Close

Fig. 11. Percentage of all contacts present in the Chloroquine material. **Fig. 12.** Main fingerprints plots from Chloroqu

3.11. Docking analysis

Molecular docking analysis of Chloroquine ligand was carried out with five structures of COVID-19 protein (PDB ID: 6M03, 5R7Y, 6W63, 5R81 and 5R84) performed using the iGEMDOCK program. The 3D structure of proteins-ligand complexes were constructed using Discovery Studio software. The goal of docking calculation is to predict the best binding orientation attraction and their protein targets while determining the activity of drug molecules. **Fig. 13** illustrates the surfaces around ligand and 2D diagrams of Chloroquine molecule with the collection of COVID-19 proteins. The different energy contributions resulting from docking calculation are grouped in **Table 8** . This table is ordered based on the total energy value which represents the sum of VDW, H-bonding and electronic interactions. With docking calculations, we have determined 10 poses. Here we present only the best pose which corresponds to minimal energies.

Chloroquine-6M03	**Chloroquine-6M03**
Chloroquine-5R7Y	**Chloroquine-5R7Y**
Chloroquine-6W63	**Chloroquine-6W63**
Chloroquine-5R81	**Chloroquine-5R81**
Chloroquine-5R84	**Chloroquine-5R84**

Figure 13: The best positions of the Chloroquine in the proteins 6M03, 5R7Y, 6W63, 5R81 and 5R84.

Results reveal that the interactions are mainly of two types: Van der Walls and hydrogen-bonding. The VDW energies interactions are stronger than H-bonding interactions, and all the compounds not have shown electronic interactions. **Fig. S3** presents several forms of intermolecular interactions between ligand and protein. Acceptor-donor electronic interactions allow the construction of hydrogen-bonding interactions. The docked ligand interactions with amino acids constituting the active site of the receptor are showed in fig. 13 and table 8. Total energy scores are at a very comparable level with an average energy of -73.274 kcal/mol. Among these series of complexes, the Chloroquine-6M03 displayed better inhibition when compared with others, since it was found to be the strongest binding energy (-81.866 kcal/mol). It had formed two H-bond interactions with LEU-141 and SER-144. The H-bond interaction was found to be -6.285 kcal/mol (fig. S3). Additionally, the van der Waals interactions (E=-75.581 kcal/mol) were also being formed with HIS-41, LEU-141, ASN-142, ASN-142, MET-165, GLU-166 and GLU-166 residues. Also, Chloroquine has a good binding interaction with 5R7Y protein and it exhibited the total energy score of -77.498 kcal/mol. The docking pose analysis of this complex revealed that the Chloroquine is oriented with the VDW interactions surrounded by the chains of LEU-141, ASN-142, ASN-142, MET-165, GLU-166 and GLU-166 in the 5R7Y protein (-70.605 kcal/mol). As seen from the Table 8, there are seven conventional VDW interactions between the 6W63 and the Chloroquine molecule (-70.961 kcal/mol) and only a hydrogen bond interaction (-4.203 kcal/mol). For the enzyme of PDB ID: 5R81: THR-26 form one H-bond interaction; THR-26, THR-26, HIS-41, MET-49, ASN-142, ASN-142 and GLY-143 forms seven van der Waals interactions. Finally, amino acids HIS-41, ASN-142, ASN-142, MET-165, GLU-166 and GLU-166 forms VDW interactions for PDB ID: 5R84 (-63.327 kcal/mol). The total energy score of this complex was calculated and found to be -68.216 kcal mol^{-1}. The molecular docking results suggest that the docked Chloroquine forms steady complexes with the different receptors which give minimum energy values. It reveals inhibition activity against 6M03, 5R7Y, 6W63, 5R81 and 5R84 enzymes. So, we can conclude that the Chloroquine can be considered as a potent inhibitor against COVID-19 virus.

4. Conclusions

Structural, electronic, topological and vibrational properties together with molecular docking have been studied for both enantiomeric S(-) and R(+) forms of potential antiviral to COVID-19 chloroquine (CQ) combining DFT calculations with SQMFF methodology. The theoretical structures of S(-) and R(+) forms were determined in gas phase and aqueous solution by using hybrid B3LYP/6-311++G** calculations. Energies differences between both forms in gas phase and aqueous solution are of 1.84 and 3.67 kJ/mol, respectively. Calculations in solution predict solvation energy of S(-) form and R(+) respectively of -55.07 and 59.91 kJ/mol. The presence of only four donor and acceptor H bonds groups present in structure CQ probably justifies the low solvation energy values of both forms, as compared with other antiviral agents. MK charges on the Cl1, N2, N3 and N4 atoms and AIM calculations could support the higher stability of R(+) form in solution in agreement with the higher reactivity predicted for the S(-) form in the same medium. Antiviral niclosamide evidences higher reactivity than CQ. Complete vibrational assignments of 153 vibration modes for both forms and scaled force constants have been performed for both forms. Very good concordances were found between the compared ^{1}H-NMR,^{13}C-NMR and UV-Vis spectra with the experimental ones, suggesting in both the presence of the two forms of CQ in solution.

A molecular docking study was performed to identify the potency of inhibition of Chloroquine molecule against COVID-19 virus.

This study clearly shows the antiviral effect, based on binding affinities and interactions formed between amino residues acid and candidate molecule, against COVID-19 virus. The interaction among the chloroquine molecule and COVID-19 are dominated by Van der Waals and hydrogen interactions. Hence, we can use these compounds as antibiotics to a greater extent.

Conflicts of interest

All authors declare that there are no conflicts of interest.

Acknowledgments

This work was supported with grants from CIUNT Project Nº 26/D608 (Consejo de Investigaciones, Universidad Nacional de Tucumán) and by the Ministry of Higher Education and Scientific Research of Tunisia. The authors would like to thank Prof. Tom Sundius for his permission to use MOLVIB.

Supporting Information Available: Tables S1-S11 and**Figures S1-S3** .

References

[1] M. Tariq, A.A. Al-Badr, Chloroquine, AnalyticaI Profiles of Drug Substances, Academv Press, Inc. 1984.

[2] J.M. Karle, I.L. Karle, Redetermination of the crystal and molecular structure of the antimalarial chloroquine bis(dihydrogenphosphate) dehydrate, research papers (organic compounds), Acta Cryst. C44 (1988) 1605-1608. https://doi.org/10.1107/S0108270188004652

[3] H.S. Preston, J.M. Stewart, The crystal structure of the antimalarial chloroquine diphosphate monohydrate, Journal of the Chemical Society D: Chemical Communications J. Chem. Soc. D 18 (1970) 1142-1143. https://doi.org/10.1039/C29700001142

[4] K. Nord, J. Karlsen, H.H. Tonnnesen, Photochemical stability of biologically active compounds. IX. Characterization of the spectroscopic properties of the 4-aminoquinolines chloroquine and hydroxychloroquine and of selected metabolites by absorption, fluorescence and phorporescence measurements, Photochem. Photobiol. 60 (1994) 427-431.*https://doi.org/10.1111/j.1751-1097.1994.tb05128.x*

[5] J. Nandi, S.N. Sharma, Efficacy of chloroquine in febrile Plasmodium falciparum infected children in Mewat region of Haryana, J. Commun. Dis. 32 (2) (2000) 137-143. https://pubmed.ncbi.nlm.nih.gov/11198399

[6] R. Hayward, K.J. Saliba, K. Kirk, The pH of the digestive vacuole of Plasmodium falciparum is not associated with chloroquine resistance, J. Cell Science 119 (2006) 1016-1025. https://doi: 10.1242/jcs.02795

[7] R. Bortoli, M. Santiago, Chloroquine ototoxicity, Clin. Rheumatol. 26 (2007) 1809-1810. https://doi.org/10.1007/s10067-007-0662-6

[8] C. Loup, J. Lelièvre, F. Benoit-Vical, B. Meunier, Trioxaquines and Heme-Artemisinin adducts inhibit the in vitro formation of hemozoin better than chloroquine, Antimicrob. Agents Chemother. 51(10) (2007) 3768–3770. https://doi:10.1128/AAC.00239-07

[9] R.G. Cooper, T. Magwere, Chloroquine has not disappeared, African health sciences 7 (2007) 185-186. https://doi: 10.5555/afhs.2007.7.3.185

[10] N. Valecha, H. Joshi, P.K. Mallick, S.K. Sharma, A. Kumar, P.K. Tyagi, B. Shahi, M.K. Das, B.N. Nagpal, A.P. Dash, Low efficacy of chloroquine: time to switchover to artemisinin-based combination therapy for falciparum malaria in India, Acta Trop. 111 (2009) 21-28. https://doi: 10.1016/j.actatropica.2009.01.013

[11] F.A. Rojas and V.V. Kouznetsov, Property-based design and synthesis of new chloroquine hybrids via simple incorporation of 2-imino-thiazolidin-4-one or 1h-pyrrol-2,5-dione fragments on the 4-amino-7-chloroquinoline side chain, J. Braz. Chem. Soc. 22 (9) (2011) 1774-1781. http://dx.doi.org/10.1590/S0103-50532011000900021

[12] M.F. Marmor, U. Kellner, T.Y.Y. Lai, J.S. Lyons, W.F. Mieler, Revised recommendations on screening for chloroquine and hydroxychloroquine retinopathy, Ophthalmology 118(2) (2011) 415-422. http://doi: 10.1016/j.ophtha.2010.11.017

[13] M.E. Egger, J.S. Huang, W. Yin, K.M. McMasters, L.R. McNally, Inhibition of autophagy with chloroquine is effective in melanoma, J. Surg. Res. 184 (2013) 274-281. http://doi: 10.1016/j.jss.2013.04.055

[14] T. Kimura, Y. Takabatake, A. Takahashi, Y. Isaka, Chloroquine in cancer therapy: a double-edged sword of autophagy, Cancer Res. 73 (2013) 3-7. http://doi: 10.1158/0008-5472.CAN-12-2464

[15] S. Hangartner, S. Eggert, F. Dussy, D. Wyler, T. Briellmann, Chloroquine and diazepam for her last sleep, Drug Test. Anal. 5 (2013) 777-780. http://doi: 10.1002/dta.1509

[16] R. Thomé, S. Costa Pinto Lopes, F.T. Costa, L. Verinaud, Chloroquine: modes of action of an undervalued drug, Immunol. Lett. 153 (2013) 50-57. http://doi: 10.1016/j.imlet.2013.07.004

[17] E. Tönnesmann, R. Kandolf, T. Lewalter, Chloroquine cardiomyopathy - a review of the literature, Immunopharmacol. Immunotoxicol. 35 (2013) 434-442. http://doi: 10.3109/08923973.2013.780078

[18] S. Doddaga, R. Peddakonda, Chloroquine-N-oxide, a major oxidative degradation product of chloroquine: identification, synthesis and characterization, J. Pharm. Biomed. Anal. 81-82 (2013) 118-125. http://doi: 10.1016/j.jpba.2013.04.004

[19] M.S. Kazi, K. Saurabh, P. Rishi, E. Rishi, Delayed onset chloroquine retinopathy presenting 10 years after long-term usage of chloroquine, Middle East Afr J Ophthalmol. 20 (2013) 89-91. http://www.meajo.org/text.asp?2013/20/1/89/106404

[20] X. Zhang, Y. Yang, X. Liang, X. Zeng, Z. Liu, W. Tao, X. Xiao, H. Chen, L. Huang, L. Mei, Enhancing therapeutic effects of docetaxel-loaded dendritic copolymer nanoparticles by co-treatment with autophagy inhibitor on breast cancer, Theranostics 4(11) (2014) 1085-1095. http://doi: 10.7150/thno.9933

[21] J-P Routy, J.B. Angel, M. Patel, C. Kanagaratham, D. Radzioch, I. Kema, N. Gilmore, P. Ancuta, J Singer, M-A Jenabian, Assessment of chloroquine as a modulator of immune activation to improve CD4 recovery in immune nonresponding HIV-infected patients receiving antiretroviral therapy, HIV Medicine 16 (2015) 48–56. http://doi: 10.1111/hiv.12171.

[22] E.B. Golden, H-Y Cho, F.M. Hofman, S.G. Louie, A.H. Schönthal, T.C. Chen, Quinoline-based antimalarial drugs: a novel class of autophagy inhibitors, Neurosurg. Focus 38 (3):E12 (2015) 1-9. http://doi: 10.3171/2014.12.FOCUS14748

[23] M.F. Marmor, U. Kellner, T.Y. Lai, J.S. Lyons, R.B. Melles, W.F. Mieler, Recommendations on screening for chloroquine and hydroxychloroquine retinopathy (2016 Revision). Ophthalmology 123(6) (2016) 1386-1394. https://doi.org/10.1016/j.ophtha.2016.01.058

[24] H. Ye, M. Chen, F. Cao, H. Huang, R. Zhan, X. Zheng, Chloroquine, an autophagy inhibitor, potentiates the radiosensitivity of glioma initiating cells by inhibiting autophagy and activating apoptosis, BMC Neurology 16 (2016) 178. https://10.1186/s12883-016-0700-6

[25] A-R Choi, J-H Kim, Y-W Woo, H.S. Kim, S. Yoon, Anti-malarial drugs primaquine and chloroquine have different sensitization effects with anti-mitotic drugs in resistant cancer cells, Anticancer Research 36(4) (2016) 1641-1648. http://ar.iiarjournals.org/content/36/4/1641

[26] L.Y. Chan, J.D.W. Teo, K.S-W Tan, K. Sou , W.L. Kwan, C-L.K. Lee, Near infrared fluorophore-tagged chloroquine in plasmodium falciparum diagnostic imaging, Molecules 23 (2018) 2635. https://doi:10.3390/molecules23102635

[27] T. Herraiz, H. Guillén, D. González-Peña, V.J. Arán, Antimalarial quinoline drugs inhibit β-hematin and increase free hemin catalyzing peroxidative reactions and inhibition of cysteine proteases,*www.nature.com/scientificreports*, 9 (2019) *15398 https://doi.org/10.1038/s41598-019-51604-z*

[28] Available from internet: //D:/CHLOROQUINE/Articles/Coronavirus%20disease%202019%20(COVID-19).pdf. Pag. 53,80.

[29] T. Frosch, M. Schmitt, G. Bringmann, W. Kiefer, J. Popp, Structural analysis of the anti-malaria active agent chloroquine under physiological conditions, J Phys Chem B 111(7) (2007) 1815-1822. https://doi: 10.1021/jp065136j

[30] M. Asghari-Khiavi, J. Vongsvivut, I. Perepichka, A. Mechler, B.R. Wood, D. McNaughton, D.S. Bohle, Interaction of quinoline antimalarial drugs with ferriprotoporphyrin IX, a solid state spectroscopy study, J. Inorg. Biochem. 105(12) (2011) 1662–1669. https://doi:10.1016/j.jinorgbio.2011.08.005

[31] M. Kozicki, D.J. Creek, A. Sexton, B.J. Morahan, A Wesełucha-Birczyńska, B.R. Wood, An attenuated total refection (ATR) and Raman spectroscopic investigations into the effects of chloroquine on Plasmodium falciparum-infected red blood cells, Analyst. 140(7) (2015) 2236-2246. https://doi: 10.1039/c4an01904k

[32] E.C. Tackman, M.J. Trujillo, T-L.E. Lockwood, G. Merga, M. Lieberman, J.P. Camden, Identification of substandard and falsified antimalarial pharmaceuticals chloroquine, doxycycline, and primaquine using surface-enhanced Raman scattering, Anal. Methods 10 (2018) 4718-4722.*https://doi.org/10.1039/C8AY01413B*

[33] A.D. Becke, Density-functional exchange-energy approximation with correct asymptotic behaviour, Phys. Rev. A38 (1988) 3098-3100. https://doi.org/10.1103/PhysRevA.38.3098

[34] C. Lee, W. Yang, R.G. Parr, Development of the Colle-Salvetti correlation-energy formula into a functional of the electron density, Phys. Rev. B37 (1988) 785-789. https://doi.org/10.1103/PhysRevB.37.785

[35] S. Miertus, E. Scrocco, J. Tomasi, Electrostatic interaction of a solute with a continuum. A direct utilization of AB initio molecular potentials for the prevision of solvent effects, Chem. Phys. 55 (1981) 117–129. https://doi.org/10.1016/0301-0104(81)85090-2

[36] J. Tomasi, J. Persico, Molecular interactions in solution: an overview of methods based on continous distributions of the solvent, Chem. Rev. 94 (1994) 2027-2094. https://doi.org/10.1021/cr00031a013

[37] A.V. Marenich, C.J. Cramer, D.G. Truhlar, Universal solvation model based on solute electron density and a continuum model of the solvent defined by the bulk dielectric constant and atomic surface tensions,

J. Phys. Chem. B113 (2009) 6378-6396. https://doi.org/10.1021/jp810292n

[38] P. Pulay, G. Fogarasi, G. Pongor, J.E. Boggs, A. Vargha, Combination of theoretical ab initio and experimental information to obtain reliable harmonic force constants. Scaled quantum mechanical (QM) force fields for glyoxal, acrolein, butadiene, formaldehyde, and ethylene, J. Am. Chem. Soc. 105 (1983) 7073-7047.*https://doi.org/10.1021/ja00362a005*

[39] G. Rauhut, P. Pulay, Transferable scaling factors for density functional derived vibrational force fields, J. Phys. Chem. 99 (1995) 3093-3100,*https://doi.org/10.1021/j100010a019*

[40] T. Sundius, Scaling of ab-initio force fields by MOLVIB. Vib. Spectrosc. 29 (2002) 89-95.*https://doi.org/10.1016/S0924-2031(01)00189-8*.

[41] R.G. Parr, R.G. Pearson, Absolute hardness: companion parameter to absolute electronegativity, J. Am. Chem. Soc. 105 (1983) 7512-7516.

https://doi.org/10.1021/ja00364a005.

[42] M.B. Márquez, S.A. Brandán, A structural and vibrational investigation on the antiviral deoxyribonucleoside thymidine agent in gas and aqueous solution phases, International J. of Quantum Chem. 114 (3) (2014) 209-221. https://doi.org/10.1002/qua.24545

[43] D. Romani, M.J. Márquez, M.B. Márquez, S.A. Brandán, Structural, topological and vibrational properties of an isothiazole derivatives series with antiviral activities, J. Mol. Struct. 1100 (2015) 279-289.*http://dx.doi.org/10.1016/j.molstruc.2015.07.038*

[44] M.A. Iramain, S.A. Brandán, Structural and vibrational study on the acid, hexa-hydrated and anhydrous trisodic salts of antiviral drug Foscarnet, Drug Des. Int. Prop. Int. J. 1(3) (2018) 1-17. https://doi:10.32474/DDIPIJ.2018.01.000114

[45] D. Romani, S.A. Brandán, Effect of the side chain on the properties from cidofovir to brincidofovir, an experimental antiviral drug against to Ebola virus disease, Arabian J. Chem. 12 (2019) 2959–2972.*http://dx.doi.org/10.1016/j.arabjc.2015.06.030*

[46] D. Romani, O. Noureddine, N. Issaoui, S.A. Brandán, Properties, reactivities and molecular docking of potential antiviral to treatment of COVID-19 niclosamide in different media, Biointerface Research in Applied Chemistry 10(6) (2020) 7295-7328.*https://doi.org/10.33263/BRIAC106.72957328*.

[47] S. Brandán, Normal internal coordinates, Force fields and vibrational study of Species Derived from Antiviral adamantadine, J. of Quantum Chem. In Press (2020)*https://doi.org/10.1002/qua.26425*.

[48] P. Gautret, J.C. Lagier, P. Parola, L. Meddeb, M. Mailhe, B. Doudier, J. Courjone, V. Giordanengo, V. Esteves Vieira, H. T. Dupont, S. Honoré, P. Colson, E. Chabrière, B. La Scola, J-M Rolain, P. Brouqui, D.Raoult, Hydroxychloroquine and azithromycin as a treatment of COVID-19: results of an open-label non-randomized clinical trial, Int. J. Antimicrob. Agents 105949 (2020).*https://doi.org/10.1016/j.ijantimicag.2020.105949*.

[49] J. Gao, Z. Tian, X. Yang, Breakthrough: Chloroquine phosphate has shown apparent efficacy in treatment of COVID-19 associated pneumonia in clinical studies, Biosci Trends 14(1) (2020) 72-73. https://doi: 10.5582/bst.2020.01047

[50] P. Gautret, J-C Lagier, P. Parola et al. Hydroxychloroquine and azithromycin as a treatment of COVID-19: results of an open-label non-randomized clinical trial, Int. J. Antimicrob. Agents (2020) 105949. https://doi: 10.1016/j.ijantimicag.2020.105949

[51] O. Noureddine, S. Gatfaoui, S.A. Brandán, H. Marouani, N. Issaoui, Structural, docking and spectroscopic studies of a new piperazine derivative, 1-phenylpiperazine-1,4-diium-bis (hydrogen sulfate), J. Mol. Struct. 1202 (2020) 127351. https://doi.org/10.1016/j.molstruc.2019.127351

[52] O. Noureddine, S. Gatfaoui, S.A. Brandán, A. Saagama, H. Marouani, N. Issaoui, Experimental and DFT studies on the molecular structure, spectroscopic properties, and molecular docking of 4-phenylpiperazine-1-ium dihydrogen phosphate, J. Mol. Struct. 1207 (2020) 127762. https://doi:10.1016/j.molstruc.2020.127762

[53] N. Issaoui, H. Ghalla, F. Bardak, M. Karabacak, N. A. Dlala, H.T. Flakus, B. Oujia, Combined experimental and theoretical studies on the molecular structures, spectroscopy, and inhibitor activity of 3-(2-thienyl) acrylic acid through AIM, NBO, FT-IR, FT-Raman, UV and HOMO-LUMO analyses, and molecular docking, J. Mol. Struct. 1130 (2017) 659-668. https://doi.org/10.1016/j.molstruc.2016.11.019

[54] A.B. Nielsen, A.J. Holder, Gauss View 5.0, User's Reference, GAUSSIAN Inc., Pittsburgh, PA, 2008.

[55] M.J. Frisch, G. W. Trucks, H.B. Schlegel, G.E. Scuseria, M.A. Robb, J.R. Cheeseman, G. Scalmani, V. Barone, B. Mennucci, G.A. Petersson, H. Nakatsuji, M. Caricato, X. Li, H.P. Hratchian, A.F. Izmaylov, J. Bloino, G. Zheng, J.L. Sonnenberg, M. Hada, M. Ehara, K. Toyota, R. Fukuda, J. Hasegawa, M. Ishida, T. Nakajima, Y. Honda, O. Kitao, H. Nakai, T. Vreven, J.A. Montgomery, Jr, J.E. Peralta, F. Ogliaro, M. Bearpark, J.J. Heyd, E. Brothers, K. N. Kudin, V.N. Staroverov, R. Kobayashi, J. Normand, K. Raghavachari, A. Rendell, J.C. Burant, S.S. Iyengar, J. Tomasi, M. Cossi, N. Rega, J.M. Millam, M. Klene, J.E. Knox, J.B. Cross, V. Bakken, C. Adamo, J. Jaramillo, R. Gomperts, R.E. Stratmann, O. Yazyev, A.J. Austin, R. Cammi, C. Pomelli, J.W. Ochterski, R.L. Martin, K. Morokuma, V.G. Zakrzewski, G.A. Voth, P. Salvador, J.J. Dannenberg, S. Dapprich, A.D. Daniels, O. Farkas, J.B. Foresman, J.V. Ortiz, J. Cioslowski, and D.J. Fox, Gaussian, Inc., Wallingford CT, 2009.

[56] E.M. Kosower, The Effect of Solvent on Spectra. I. A New Empirical Measure of Solvent Polarity: Z-Values, J. Am. Chem. Soc. 1958, 80, 13,*https://doi.org/10.1021/ja01546a020*

[57] Corinne M. Gray, Karthikeyan Saravanan, Guofeng Wang & John A. Keith (2017) Quantifying solvation energies at solid/liquid interfaces using continuum solvation methods, Molecular Simulation, 43:5-6, 420-427, DOI:*10.1080/08927022.2016.1273525*

[58] E.V. Katkova, A. V. Onufriev, B. Aguilar, V.B. Sulimov, Accuracy comparison of several common implicit solvent models and their implementations in the context of proteinligand binding, J Mol Graph Model. 72 (2017) 70–80. doi:10.1016/j.jmgm.2016.12.011.

[59] P. Ugliengo, MOLDRAW Program, University of Torino, Dipartimento Chimica IFM, , 1998.

[60] B.H. Besler, K.M. Merz Jr, P.A. Kollman, Atomic charges derived from semiempirical methods, J. Comp. Chem. 11 (1990) 431-439. https://doi.org/10.1002/jcc.540110404

[61] E.D. Glendening, J.K. Badenhoop, A. D. Reed, J. E. Carpenter, F. Weinhold, NBO 3.1; Theoretical Chemistry Institute, University of Wisconsin; Madison, WI, 1996.

[62] R.F.W. Bader, Atoms in Molecules, A Quantum Theory, Oxford University Press, Oxford, 1990, ISBN: 0198558651.

[63] F. Biegler-Köning, J. Schönbohm, D. Bayles. AIM2000; A Program to Analyze and Visualize Atoms in Molecules, J. Comput. Chem. 22 (2001) 545-559. https://doi.org/10.1002/1096-987X(20010415)22:5<545::AID-JCC1027>3.0.CO;2-Y

[64] R. Ditchfield, Self-consistent perturbation theory of diamagnetism. I. A gage-invariant LCAO (linear combination of atomic orbitals) method for NMR chemical shifts, Mol Phys. 27 (1974) 714–722. https://doi.org/10.1080/00268977400100711

[65] G. Keresztury, S. Holly, G. Besenyei, J. Varga, A.Y. Wang, J.R. Durig. Vibrational spectra of monothiocarbamates-II. IR and Raman spectra, vibrational assignment, conformational analysis and ab initio calculations of S-methyl-N,N-dimethylthiocarbamate Spectrochim. Acta 49A (1993) 2007-2026. https://doi.org/10.1016/S0584-8539(09)91012-1

[66] D. Michalska, R. Wysokinski, The prediction of Raman spectra of platinum(II) anticancer drugs by density functional theory, Chem. Phys. Letters 403 (2005) 211-217. https://doi.org/10.1016/j.cplett.2004.12.096

[67] S. K. Wolff, D. J. Grimwood, J. J. McKinnon, D. Jayatilaka, M. A. Spackamn, Crystal Explorer 3.1, University of Westren Australia, Perth, 2013.

[68] S. Durdagi, B. Aksoydan, B. Dogan, K. Sahin, A. Shahraki, Screening of clinically approved and investigation drugs as potential inhibitors of COVID-19 main protease: a virtual drug repurposing study, ChemRxiv. Preprint (2020) https://doi: 10.26434/chemrxiv.12032712.v1

[69] B. Shah, P. Modi, S.R. Sagar, In silico studies on therapeutic agents for COVID-19: Drug repurposing approach, Life Sci. 252 (2020) 117652. https://doi: 10.1016/j.lfs.2020.117652

[70] S. Chakraborti, N. Srinivasan, Drug repurposing approach targeted against main protease of SARS-CoV-2 exploiting 'Neighbourhood Behaviour'in 3D protein structural space and 2D chemical space of small molecules (2020) Preprint. https://doi:10.26434/chemrxiv 12057846 (2020).

[71] B. Shah, P. Modi, S.R. Sagar, In silico studies on therapeutic agents for COVID-19: Drug repurposing approach, Life Scie. (2020) 117652. https://doi.org/10.1016/j.lfs.2020.117652

[72] Srinivasan Narayanaswamy. "Drug Repurposing Approach." (2020.

[73] Available from: http://www.rcsb.org/pdb/

[74] D.S. Visualizer, Accelrys software inc. Discovery Studio Visualizer 2 (2005).

[75] J-M.Yang, C-C Chen, GEMDOCK: a generic evolutionary method for molecular docking Proteins, Struct. Funct. Bioinforma. 55 (2004) 288–304. https://doi.org/10.1002/prot.20035

[76] R.A. Rudyk, M.A. Checa, C.A.N. Catalán, S.A. Brandán, Structural, FT-IR, FT-Raman and ECD studies on the free base, cationic and hydrobromide species of scopolamine alkaloid, J Mol. Struct. 1180 (2019) 603-617. https://doi.org/10.1016/j.molstruc.2018.12.040

[77] M.E. Manzur, S.A. Brandán, S(-) and R(+) Species derived from antihistaminic promethazine agent: structural and vibrational studies, Heliyon 5 (2019) e02322.*https://doi.org/10.1016/j.heliyon.2019.e02322.*

[78] D.F. Veber. S.R. Johnson, H-Y Cheng, R. Brian, K.W. Ward, K.D. Kopple, Molecular properties that influence the oral bioavailability of drug candidates, J. Med. Chem. 45 (2002) 2615-2623. https://doi: 10.1021/jm020017n

[79] C.A. Lipinski, F. Lombardo, B.W. Dominy, P.J. Feeney, Experimental and computational approaches to estimate solubility and permeability in drug discovery and development setting, Advanced Drug Delivery Reviews 46 (2001) 3-26.*https://doi.org/10.1016/S0169-409X(00)00129-0*

[80] M. Khalid, M. Adeel, M.A. Ullah, M.U. Khan, M.N. Tahir, A.A.C. Braga, Synthesis, crystal structure analysis, spectral IR, UV–Vis, NMR assessments, electronic and nonlinear optical properties of potent quinoline based derivatives: Interplay of experimental and DFT study, J. of Saudi Chem. Soci. 23 (2019) 546–560. https://doi.org/ 10.1016/j.jscs.2018.09.006

[81] S. Gatfaoui, A. Mezni, T. Roisnel, H. Marouani, Synthesis, characterization, Hirshfeld surface analysis and antioxidant activity of a novel organic-inorganic hybrid material 1-methylpiperazine-1,4-diium bis(nitrate), J. Mol. Struct. 1139 (2017) 52-59. https://doi.org/10.1016/j.molstruc.2017.03.028

[82] S. Gatfaoui, N. Issaoui, A. Mezni, F. Bardak, T. Roisnel, A. Atac, H. Marouani, Synthesis, structural and spectroscopic features, and investigation of bioactive nature of a novel organic-inorganic hybrid material 1H-1,2,4-triazole-4-ium trioxonitrate, J. Mol. Struct. 1150 (2017) 242-257. https://doi.org/10.1016/j.molstruc.2017.08.092

[83] S. Gatfaoui, N. Issaoui, S. A. Brandán, T. Roisnel, H. Marouani, Synthesis and characterization of p-xylylenediaminium bis(nitrate).Effects of the coordination modes of nitrate groups on their structuraland vibrational properties, J. Mol. Struct. 1151 (2018) 152-168.*https://doi.org/10.1016/j.molstruc.2017.09.027*

[84] M. Tahenti, S. Gatfaoui, N. Issaoui, T. Roisnel, A tetrachlorocobaltate(II) salt with 2-amino-5-picolinium: Synthesis, theoretical and experimental characterization, J. Mol. Struct. 1207 (2020) 127781. https://doi.org/10.1016/j.molstruc.2020.127781